ADVANCED MATERIALS INTERFACES
Open Access
www.advmatinterfaces.de

Check for updates

Understanding the Growth and Properties of Sputter-Deposited Phase-Change Superlattice Films

Simone Prili, Valeria Bragaglia, Vara Prasad Jonnalagadda, Jesse Luchtenveld, Bart J. Kooi, Fabrizio Arciprete, Abu Sebastian,* and Ghazi Sarwat Syed**

Highly textured chalcogenide films have recently gained significant interest for phase-change memory applications. Several reports have highlighted that programming efficiency improves in devices featuring superlattice stacks, such as $Ge_2Sb_2Te_5/Sb_2Te_3$. However, to be technologically relevant, these films must be deposited on foundry-scale wafers using processes compatible with back end of the line (BEOL) integration and complementary metal-oxide-semiconductor (CMOS) technology, such as, for example, sputter deposition. In this work, we present our observations on the influence of temperature, pressure, and seeding layer on the sputter growth processes of superlattice films. By measuring various material properties, we construct a pseudo-phase diagram to illustrate the growth of both individual and superlattice films with different periodicities on technologically relevant substrates, namely SiO_2 and carbon. These results provide important insights into the structure, intermixing and electro-optical properties of superlattice films, and identify optimal growth parameters critical for the manufacturability via sputtering of the material.

1. Introduction

In addition to data storage, phase-change memory devices (PCM) are increasingly being applied in analog in-memory computing.[1,2] Conventional devices are usually based on untextured films of Ge-Sb-Te (GST) alloys, which are limited in performance by modest programming currents and device non-idealities. A unique solution does not exist and different approaches can be taken either at the device architecture or material level.[3–5] In the latter case, a promising solution could be found in the use of textured chalcogenide superlattices (CSL) as the active material of the device. A superlattice (SL) is defined as a periodic stack of two or more materials which, in case of PCM, are usually chalcogenides like GeTe, $Ge_xSb_yTe_z$ (GST) and Sb_2Te_3. The first investigations on $GeTe/Sb_2Te_3$ SL showed that the introduction of these materials into standard devices notably reduced the programming currents. Such reduction was initially explained supposing Ge atoms reorganization within the GeTe layers,[6] leading to a crystalline-to-crystalline transition rather than the typical amorphous-to-crystalline transition via melt quenching. However, subsequent works have shown that GeTe reacts with Sb_2Te_3 during deposition, forming GST and switching via melt-quench dynamics.[7–10] There is now growing evidence that the improvements in the device performance can be attributed to the layered nature of the CSL; more specifically, from the presence of van der Waals (vdW)-like gaps within the film. These gaps render nanoscaled electro-thermal confinements, from reduced cross-plane electrical and thermal conductivity.[11] Naturally, it is expected that the performance benefits improve with the density of these gaps (number of vdW layers divided by film thickness).

These gaps are naturally formed in materials such as Sb_2Te_3 and GST. A unit cell of Sb_2Te_3 consists of a stack of three blocks, each about 1 nm thick and composed of covalent bonded Te-Sb-Te-Sb-Te planes. Furthermore, these blocks are separated by vdW-like gaps,[12] resulting in a layered trigonal structure with a lattice parameter *c* of approximately 3 nm [13] (i.e., 3 blocks). Undesirably, Sb_2Te_3 has a low crystallization temperature, resulting in poor state retention, thus limiting its employment in device applications. In contrast, GST has a moderate crystallization temperature and, like Sb_2Te_3, its stable phase features a trigonal unit cell composed of blocks separated by vdW-like gaps. Furthermore, the mass difference of Ge with respect to Sb and Te provides a more improved thermal confinement in GST based compositions.[12] The lattice parameters of GST can vary

S. Prili, V. Bragaglia, V. P. Jonnalagadda, J. Luchtenveld, A. Sebastian, G. S. Syed
IBM Research – Europe
Säumerstrasse 4, Rüschlikon 8803, Switzerland
E-mail: prili@roma2.infn.it; ase@zurich.ibm.com; ghs@zurich.ibm.com

S. Prili, F. Arciprete
Department of Physics
University of Rome "Tor Vergata"
Via della Ricerca Scientifica 1, Rome 00133, Italy

S. Prili, F. Arciprete
Institute for Microelectronics and Microsystems (CNR–IMM)
Via del Fosso del Cavaliere 100, Rome 00133, Italy

J. Luchtenveld, B. J. Kooi
Zernike Institute for Advanced Materials
University of Groningen
Nijenborgh 4, AG Groningen 9747, Netherlands

The ORCID identification number(s) for the author(s) of this article can be found under https://doi.org/10.1002/admi.202500058

© 2025 The Author(s). Advanced Materials Interfaces published by Wiley-VCH GmbH. This is an open access article under the terms of the Creative Commons Attribution License, which permits use, distribution and reproduction in any medium, provided the original work is properly cited.

DOI: 10.1002/admi.202500058

21967350, 0, Downloaded from https://advanced.onlinelibrary.wiley.com/doi/10.1002/admi.202500058 by Cochraneltalia, Wiley Online Library on [09/05/2025]. See the Terms and Conditions (https://onlinelibrary.wiley.com/terms-and-conditions) on Wiley Online Library for rules of use; OA articles are governed by the applicable Creative Commons License

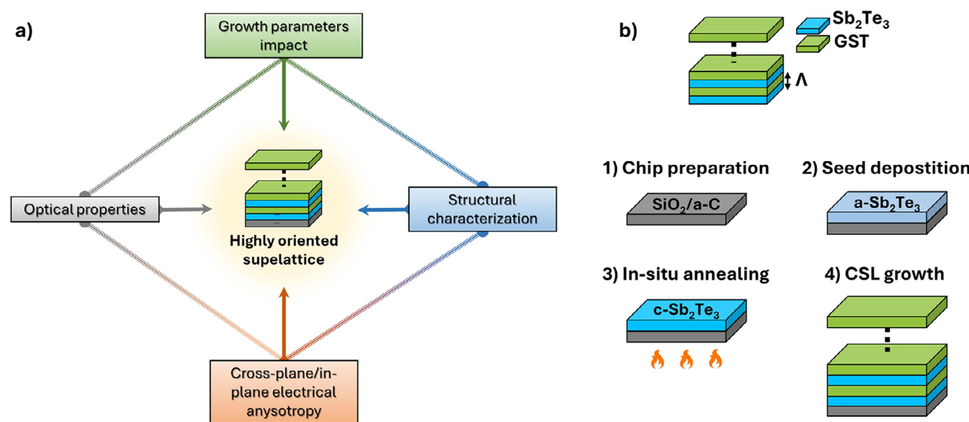

Figure 1. a) An overview of the methods used to study the growth of highly oriented superlattice films; b) Schematics illustrating the two-step deposition scheme of the superlattice films.

depending on the stoichiometry, with each block consisting of alternating Te and Ge/Sb planes.[14] For example, similarly to Sb_2Te_3, in case of GST 124, the trigonal unit cell is composed of three blocks of 7 Ge-Sb-Te planes. Conversely, GST 225 features a unit cell consisting in one block of 9 Ge-Sb-Te planes.

As a result, the larger block size (1.8 nm for GST 225) suggest that the density of vdW-like gaps in a textured GST film would be constrained. This fundamentally presents the benefits of CSL comprised of both GST and Sb_2Te_3, with however an important caveat. If a CSL is created with periods containing incomplete blocks, such as depositing only half a block of Sb_2Te_3, intermixing with the subsequent GST block may occur. This can lead to the formation of larger GST blocks or even not layered GST, which undesirably reduces the density of gaps and affects performance improvements.[15] Therefore, it is imperative to grow CSL of high quality in which such intermixing effects are reduced. In this context, although much work has been done to investigate the growth of GeTe/Sb_2Te_3 CSL with various techniques,[8,16–24] a systematic study on the sputter growth processes of GST/Sb_2Te_3 type CSL is still lacking. This is particularly relevant, as GST-based superlattices not only show a reduced tendency to intermix compared to their GeTe-based counterparts,[25] but have also demonstrated promising results in actual devices.[26,27]

Considering its typical use in BEOL for wafer scale deposition, here we investigate Ar^+ sputter deposition for growth of GST/Sb_2Te_3 superlattices on SiO_2 and C substrates (see **Figure 1a**). Specifically, we carefully separate the effects of temperature (*T*) and pressure (*p*), creating a *p*-*T* diagram that serves as a framework for growing highly ordered GST and Sb_2Te_3 films, as well as CSLs with various periodicities. We utilized spectroscopic ellipsometry to monitor bandgap changes with periodicity, X-ray diffraction (XRD) for structural characterization, modified transfer length measurements (m-TLM) to analyze resistivity, and transmission electron microscopy (TEM) to examine the crystal structure and intermixing effects.

2. Results

We used a two-step approach for the deposition of CSL films.[11,16,28] This process, as illustrated in Figure 1b, involves first depositing a few nanometers thick layer of Sb_2Te_3 at room temperature (seed layer). Subsequently, the sample is heated to the growth temperature (T_{growth}) at which the rest of the film stack is deposited. This procedure is critical for two reasons: first, it initiates the crystallization of the seed layer, resulting in a Te-terminated surface suitable for Sb_2Te_3 vdW epitaxy; secondly, the elevated temperature facilitates the surface diffusion of incoming atoms, thereby promoting the growth of a crystalline film. In the following sections, we develop an understanding of these growth processes. We detail the growth of Sb_2Te_3 and $Ge_2Sb_2Te_5$ in separate sections, which leads to an understanding of the optimal parameters for GST/Sb_2Te_3 CSL deposition.

2.1. An Understanding of Sb_2Te_3 deposition

As illustrated in **Figure 2a**, the crystal structure of stoichiometric Sb_2Te_3 consists of vertically stacked Te-Sb-Te-Sb-Te quintuple layers (QLs) separated by vdW gaps. However, during high-temperature growth, desorption kinetics may be favored, leading to the formation of non-stoichiometric films. In the case of Sb_2Te_3, this often results in Sb-rich films that include Sb_2 double layers (DLs) intercalated between the Sb_2Te_3 QLs, as shown in Figure 2a. This deviation can affect both the properties of the alloy as well as the characteristics of the superlattices.[17]

In the first experiment, the effect of a seed layer on the growth of Sb_2Te_3 was evaluated by fabricating Sb_2Te_3 films at T_{growth} = 200 °C, with and without a 3 nm thick seed layer (this is detailed in Supporting Information Section S1). We found that films without seed layers exhibited spurious orientations (non-(00ℓ) diffraction peaks). Therefore, the absence of Te-terminated surfaces was noted to be detrimental to the epitaxial growth of Sb_2Te_3, indicating the fundamental requirement for a seeding layer. In the second experiment, the effect of seed layer thickness (up to 5 nm) was investigated. We observed 3 nm to be the optimal thickness for the seed layer, as the intensity of the diffraction peaks, indicative of higher crystal quality, diminished with increasing thickness (see Supporting Information Section S1).

To investigate how Te desorption is related to sputter growth parameters, we grew Sb_2Te_3 films under different pressures *p* (3/6/9 µbar) and analyzed their structure using XRD, as shown

© 2025 The Author(s). Advanced Materials Interfaces published by Wiley-VCH GmbH

21967350, 0, Downloaded from https://advanced.onlinelibrary.wiley.com/doi/10.1002/admi.202500058 by Cochraneltalia, Wiley Online Library on [09/05/2025]. See the Terms and Conditions (https://onlinelibrary.wiley.com/terms-and-conditions) on Wiley Online Library for rules of use; OA articles are governed by the applicable Creative Commons License

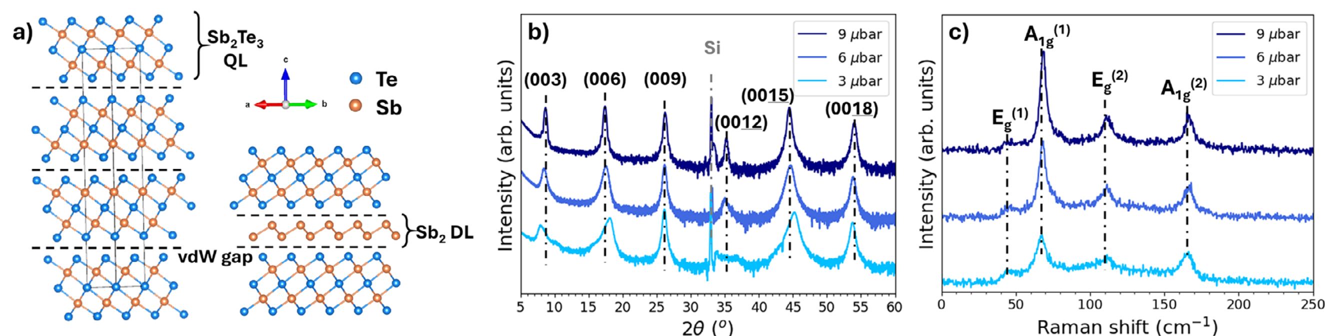

Figure 2. a) Computed crystal structures of stoichiometric Sb_2Te_3 (left panel) and Sb_2 bilayers intercalated due to Sb enrichment (right panel); b) XRD patterns of Sb_2Te_3 films grown at 200 °C under different *p* conditions; c) Raman spectra of Sb_2Te_3 films grown at 200 °C with varying *p* values.

in Figure 2b. We make a few observations. The first is that the introduction of a seed layer consistently results in Sb_2Te_3 films exhibiting (00ℓ)-only diffraction peaks, associated with proper orientation, regardless of the pressure. However, at lower pressures, these peaks broaden and shift: particularly the (003), (006), and (0015) reflections, while the (0012) peak disappears for 3 µbar case. This trend can be well attributed to an enrichment of Sb, which accumulates as double layers (DLs) between Sb_2Te_3 quintuple layers.[29] Interestingly, due to the vdW nature of Sb_2 double layers,[30] the desired out-of-plane orientation remains preserved even if the overall material is no longer stoichiometric. This observation is further supported by the Raman spectra of the same films shown in Figure 2c. The film deposited at 9 µbar shows clear peaks at 68 cm^{-1}, 112 cm^{-1}, and 167 cm^{-1}, corresponding to the Sb_2Te_3 $A_{1g}^{(1)}$, $E_g^{(2)}$, and $A_{1g}^{(2)}$ modes, respectively, along with a small bump at ≈ 46 cm^{-1}, which could be associated with $E_g^{(1)}$ mode.[31] As the pressure decreases, we observe a significant reduction in the intensity of the $A_{1g}^{(1)}$ and $E_g^{(2)}$ modes, with the 3 µbar film showing a red shift to 67 cm^{-1} and 110 cm^{-1}, respectively. Notably, the $E_g^{(2)}$ mode does not exhibit the same behavior. This particular phenomenon has been experimentally and theoretically shown to result from the introduction of Sb_2 layers between Sb_2Te_3 quintuple layers,[29] thus verifying the formation of DL.

To further explore Sb enrichment, we deposited Sb_2Te_3 films across a broad temperature range (180-240 °C), at working pressures of 9 µbar and 6 µbar. The diffraction patterns of the resulting samples are shown in **Figure 3**a,b. We observed that the out-of-plane orientation in the films remains consistent regardless of the (*p*, *T*) conditions. However, films grown at lower pressures exhibit systematic broadening and slight shifts with increasing temperature. The (003), (006), and (0015) peaks, being the most sensitive to these variations, were fitted with pseudo-Voigt curves to determine their 2θ positions. These positions were used to monitor Sb enrichment and are plotted as a function of temperature and pressure in Figure 2c (dashed lines represent the 2θ positions for Sb_2Te_3 grown at 9 µbar and 200 °C). It is evident that, within the given temperature range, pressure has an observable effect on desorption phenomena. Specifically, for films deposited

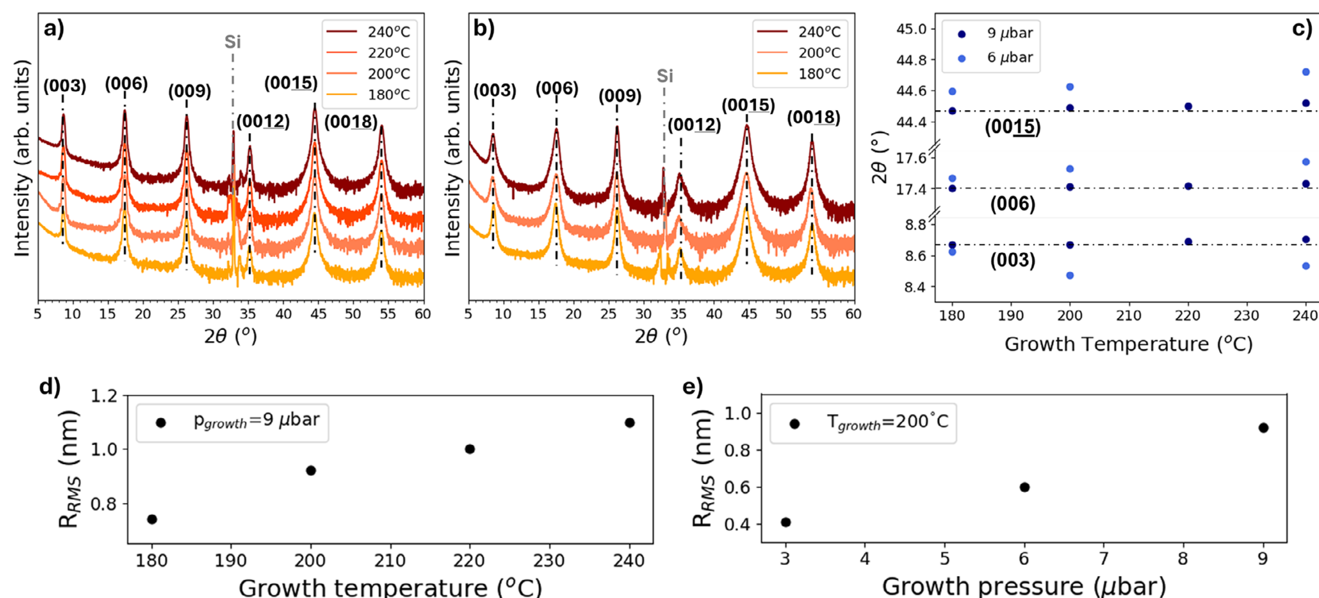

Figure 3. XRD curves of Sb_2Te_3 films grown at 9 µbar (a) and 6 µbar (b) under various T_{growth}; c) 2θ peak positions of (00ℓ) Sb_2Te_3 reflections as a function of T_{growth} at 9 µbar (dark blue) and 6 µbar (light blue). The film roughness as a function of temperature (d) and pressure (e).

© 2025 The Author(s). Advanced Materials Interfaces published by Wiley-VCH GmbH

21967350, 0, Downloaded from https://advanced.onlinelibrary.wiley.com/doi/10.1002/admi.202500058 by Cochraneltalia, Wiley Online Library on [09/05/2025]. See the Terms and Conditions (https://onlinelibrary.wiley.com/terms-and-conditions) on Wiley Online Library for rules of use; OA articles are governed by the applicable Creative Commons License

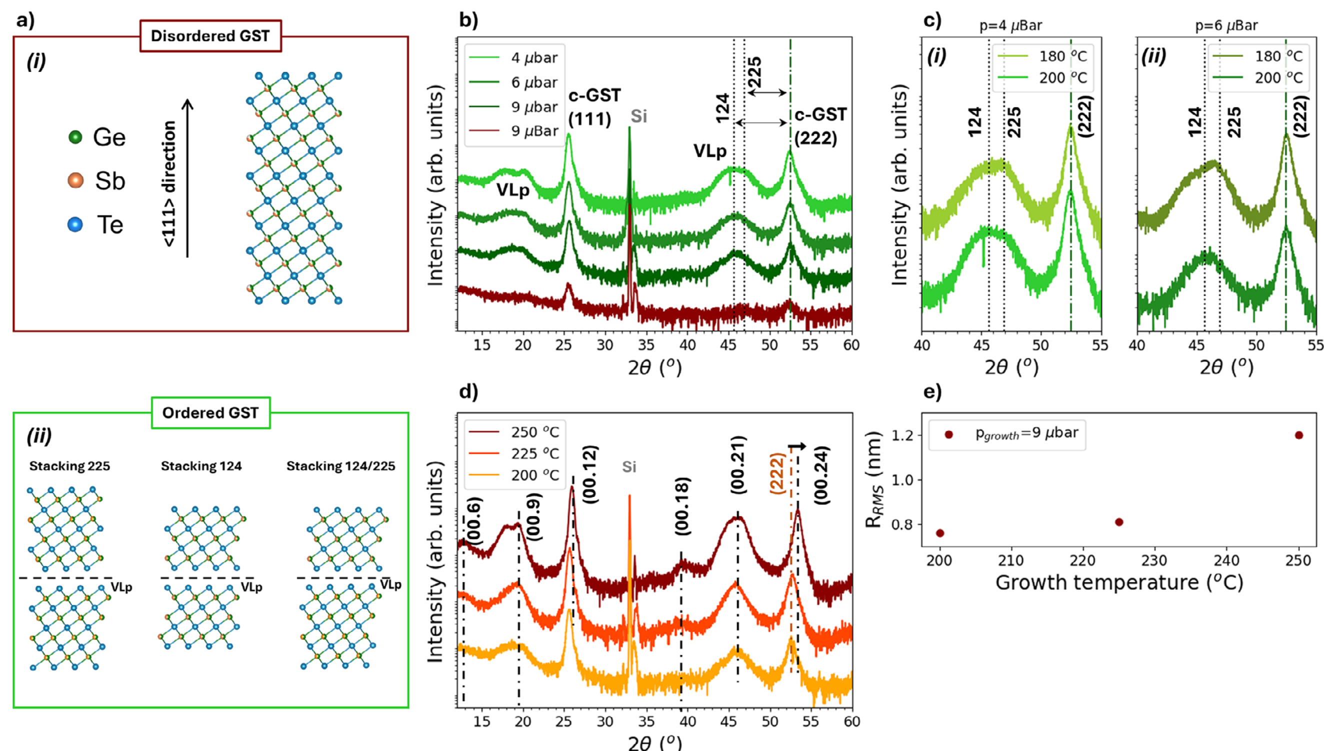

Figure 4. a) Computed structures of different cubic GST phases viewed with [111] axes in the vertical direction: ordered GST phases featuring 124, 225 and mixed 124-225 stacking (green box) and disordered cubic GST with vacancies randomly distributed in one sublattice (red box); b) XRD curves of GST films grown at 200 °C and different p values. Red curve refer to a film grown without seed layer while green ones refer to samples featuring seed layer; c) Detail of GST 2nd diffraction order for films deposited with different T and p values; d) XRD curves of GST films grown at 9 μbar and increasing T_{growth}; dashed black lines indicate t-GST reflections while (222) c-GST peak is indicated by a orange line; **e)** surface roughness measured at different values of T_{growth}.

at 9 μbar, the 2θ shift from 180 °C to 240 °C is minimal and up to T < 220 °C, a lattice parameter of 3.0519 ± 0.0006 nm is observed, which is close to stoichiometric Sb_2Te_3.[32] In contrast, at lower pressures, the 2θ shift is more pronounced: films grown at 6 μbar, 180 °C are poorer in Te compared to those grown at 9 μbar, 240 °C.

Given that the films must be grown on large-scale wafers, surface roughness becomes a crucial parameter. Rough films can lead to delamination issues during device fabrication and, in the case of CSL, may additionally degrade the interface quality when stacking GST and Sb_2Te_3 layers. Root mean square roughness (R_{rms}) obtained from AFM tomographies of Sb_2Te_3 films grown at varying p and T is reported in Figure 3d,e. It is observed that while high p enhances Te content, it also results in rougher films. Similarly, although high T improves film crystallinity (evidenced by more intense XRD peaks), it also leads to increased surface roughness. Consequently, we find that when working with a stoichiometric target, there is no single ideal growth condition. For instance, it is possible to grow highly ordered, stoichiometric Sb_2Te_3 films from a stoichiometric target by minimizing Te desorption, as well as the Sb intercalation between Sb_2Te_3 QLs through optimal selection of (p, T) conditions. However, this is achieved at the expense of increased film roughness.

In sum, all these findings can be summarized as follows. A seed layer enhances the [001] out-of-plane orientation in Sb_2Te_3 films and reduces spurious orientations, with an optimal thickness of 3 nm. In the typical temperature range used for growing phase change alloys, pressure is crucial for controlling Te desorption, allowing for various compositions. By fine-tuning (p and T), stoichiometric Sb_2Te_3 films can be produced from stoichiometric targets with controlled Sb enrichment. Higher pressure and temperature enhance film stoichiometry and crystallinity but increase surface roughness, requiring trade-offs when designing process conditions.

2.2. An understanding of Ge-Sb-Te deposition

Besides its thermodinamically stable trigonal structure, GST also features a metastable rock-salt cubic (c-) phase which is the one generally formed during electrical switching in a PCM device. It consists of alternating layers of Te and Ge/Sb/vacancies stacked along the [111] direction.[33,34] Depending on the distribution of vacancies, two possible phases can be obtained: a disordered phase, where vacancies are randomly distributed in the cation sublattice, and an ordered phase, where vacancies accumulate in layers (representing depleted Sb/Ge planes), known as vacancy layers (VL).[35,36] Crucially, the formation of these vacancy layers divides the c-GST into distinct blocks, with their size depending on the number of Te and Ge/Sb planes between two vacancy layers. **Figure 4a** illustrates the computed structures of disordered c-GST *(i)* and ordered c-GST *(ii)*, showing different stacking

© 2025 The Author(s). Advanced Materials Interfaces published by Wiley-VCH GmbH

ADVANCED MATERIALS INTERFACES
Open Access
www.advmatinterfaces.de

configurations. Unlike Sb_2Te_3, the formation of VL in c-GST is understood to precede the creation of the vdW gaps of t-GST.[35–37]

In the first experiment, we investigate the role of the Sb_2Te_3 seed layer in the growth of GST, as well as the effect of deposition pressure. XRD curves of GST films (≃ 20–25 nm thick) deposited at T_{growth} of 200 °C under different pressures, with (green curves) and without (red curves) the seed layer, are shown in Figure 4b. Seeding the substrate surface with Sb_2Te_3 clearly results in higher quality crystalline films, as indicated by the overall increased intensity of the diffraction peaks. The peaks at ≃ 25.6° and 52.7°, detected in all cases, identify the as-grown films as cubic GST with complete [111] out-of-plane orientation. Furthermore, while GST deposited without a seed layer grows in the disordered phase, films grown with a seed layer exhibit distinct peaks at approximately 19° and 45.5°, indicating the formation of VL.[36]

Using this data, we further estimate (this is detailed in Supporting Information Section S2) the predominant GST stacking-type by measuring the separation, Δq (where $q = 4\pi \sin(\theta)/\lambda$), between the (222) GST reflection and the vacancy layers peaks (VLp). This is computed, even in case of GeTe-rich compositions, as $2\pi/\Delta q$.[38,39] We note that although the films were grown using a stoichiometric GST 225 target, the vacancy layer peak (VLp) for films grown at 200 °C under 9 µbar and 6 µbar yield $\Delta q = 0.43$ Å^{-1}, which is suggestive of a predominant c-GST 124 stacking. In contrast, films grown at (4 µbar) exhibit significantly broader VLp peaks. This broadening is also observed for films deposited at 180 °C under4-6 µbar (as detailed in Figure 4c). In these cases the VLp are fitted by two Gaussians: one with $\Delta q = 0.36$–0.38 Å^{-1}, that is compatible with c-GST 225, and another that could be linked to minor c-GST 124. Interestingly, while films grown at 4 µbar display this mixed stacking at both 180 °C and 200 °C (see Figure 4c(i)), under 6 µbar (Figure 4c(ii)) the same phenomena is observed only at 180 °C. In fact, increasing T_{growth} to 200–225 °C result in films characterized by 124 stacking as can be observed in Figure 4d. This suggests that unlike Sb_2Te_3, where p was the most relevant parameter to influence film growth, in case of GST the growth temperature plays a crucial role as it influences the overall stacking of c-GST, favoring GST 124 at higher T. Moreover, in case of $T_{growth} = 250$ °C former GST (111) and (222) peaks shift noticeably from their original positions (25.65° and 52.66°, see Figure 4d) to 25.93° and 53.32°, respectively. This shift, along with the appearance of additional features in the diffractogram, indicates that the film grows in the trigonal rather than the cubic phase.[40,41] The emergence of the trigonal phase at a higher temperature aligns with its known tendency to crystallize at higher temperatures compared to the cubic phase. This observation is further corroborated by film's roughness (Figure 4e) as a function of T_{growth}. As long as the cubic phase is grown, R_{rms} changes very little as function of T_{growth} (R_{rms} = 0.76 nm -0.81 nm); however, when the t-GST formation is triggered, R_{rms} raises significantly to 1.2 nm (at 250 °C).

Comparing these findings with the results on Sb_2Te_3, we observe that, in the case of GST, temperature rather than pressure seems to have a more significant effect on the film's structure. This is possibly due to the presence of Ge atoms during growth that have been suggested to preferentially bond with Te.[38] This is consistent with our results, as it suggests that the presence of Ge stabilizes Te adsorption, thereby reducing the impact of pressure on its desorption. In sum, the key observations are the following: a Sb_2Te_3 seed layer (thus, Sb_2Te_3) enables the growth of ordered c-GST, pressure does not have significant effect on the growth, but c-GST of different stacking-types, as well as t-GST can be obtained starting from a stoichiometric GST 225 target by fine-tuning T_{growth}. Concerning roughness, as long as the c-GST phase is obtained, the as grown films experience minor R_{rms} variations as function of temperature and are smoother than Sb_2Te_3 films grown in the same conditions. On the other hand, if t-GST is grown, due to its fiber textured nature, R_{rms} increases significantly.

2.3. An Understanding of GST/Sb_2Te_3 Superlattices Growth

The observations gathered for the growth of Sb_2Te_3 and GST films can now be combined to draw a (p,T) phase diagram (see **Figure 5a**), which can point to the conditions that can yield highly textured films with stoichiometric composition and low surface roughness (R_{rms}<1 nm). This phase diagram, also serves as the starting point for the growth of CSL films. For Sb_2Te_3, stoichiometric films can be grown at 9 µbar (or higher), with low dependence on T_{growth}. However, above 220 °C, the surface roughness exceeds 1 nm, so this temperature is considered the upper bound for CSL deposition at this pressure. At 3 µbar, despite the low roughness, notable Te desorption occurs, making it unsuitable. At 6 µbar, despite moderate Te desorption, good quality films can be obtained within the low T_{growth} range. For GST, the pressure in the investigated range has a marginal effect on film quality. In terms of T_{growth}, except at 250 °C, the films maintain low roughness under the same (p,T) conditions as Sb_2Te_3. This indicates that the GST growth window favorably overlaps with the region where high-quality Sb_2Te_3 is obtained, allowing for more streamlined parameter optimization for CSL deposition.

We start off with investigating the impact of pressure (up to 12 µbar) on the CSL growth. Using XRD, we find (the analysis of diffraction curves Supporting Information section S3) that textured CSL films can be grown under all p conditions. However, CSL films grown at lower p_{growth} values (e.g., 6 µbar) exhibits broader peaks. We are able to attribute this to Te desorption in Sb_2Te_3 (see Sb_2Te_3 section and ref. [17]). Nonetheless, we note that while higher p_{growth} improves the overall structural quality, it negatively impacts CSL surface morphology. SEM images (see Figure 5b) show a gradual increase in number of flakes (bright features) as p_{growth} increases. This effect is particularly evident for CSL grown at 9 µbar, where the inset reveals numerous hexagonal and triangular flakes indicative of the trigonal structure characteristic of Sb_2Te_3 and GST. Interestingly, this phenomenon occurs only in the case of CSL: GST and Sb_2Te_3 films grown under the same (p,T) conditions have smoother surfaces, as noted in the SEM and AFM analysis (see Supporting Information Section S3).

Furthermore, the influence of the seed layer was investigated in the growth of CSL films. Figure 5c shows the XRD curves of superlattices (3 nm Sb_2Te_3/ 1.8 nm GST) deposited at 180 °C on: bare SiO_2 (red), SiO_2 covered by 3 nm and 5 nm thick seed layer deposited at 180 °C (orange and green), as well as on SiO_2 coated by 3 nm thick seed deposited at RT. Depositing the CSL directly on the bare substrate results in a film with a XRD curve (red)

© 2025 The Author(s). Advanced Materials Interfaces published by Wiley-VCH GmbH

21967350, 0, Downloaded from https://advanced.onlinelibrary.wiley.com/doi/10.1002/admi.202500058 by Cochraneltalia, Wiley Online Library on [09/05/2025]. See the Terms and Conditions (https://onlinelibrary.wiley.com/terms-and-conditions) on Wiley Online Library for rules of use; OA articles are governed by the applicable Creative Commons License

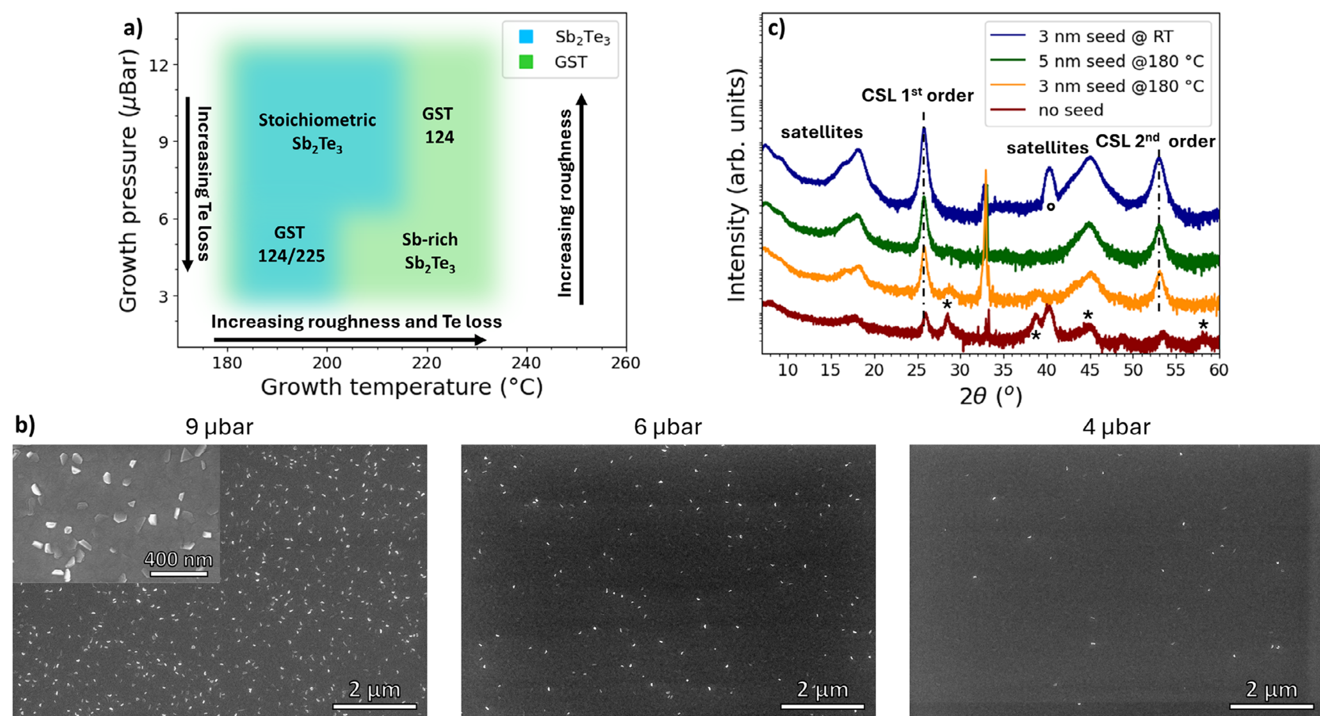

Figure 5. a) (p,T) phase diagram illustrating growth conditions for GST (green) and Sb_2Te_3 (blue) films; b) SEM images of CSL films grown at different p_{growth} values. The inset illustrates flakes, indicative of delaminated Sb_2Te_3 and GST grains; c) XRD curves of CSL deposited without seed layer (red curve), with 3 nm RT seed layer (topmost blue curve) and 3 nm and 5 nm thick high T_{growth}- deposited seed layer (second and third curve from the bottom respectively).

characterized by a number of low intensity peaks, most of which are not related to the a superlattice structure. Peaks marked by "*" at ≃ 28.7° and 39° originate from non (00.ℓ) t-GST planes[42] while those at ≃ 25.8 and 53.3 from (00.ℓ) t-GST[40] that grows without preferential orientation. The faint peaks at ≃ 17.5°, 44.8° belong to Sb_2Te_3 (006) and (0015) planes respectively (see fig. 2) while the one marked by a circle is a W cap layer. In conclusion, a CSL is not obtained. On the other hand, introducing the optimized 3 nm seed layer at RT, as observed for the films deposited at different p, the resulting film shows a diffraction curve (blue) in which the main CSL peaks, as well as its satellites, are clearly observed. Undesirably, depositing an amorphous seed layer that is later crystallized through annealing can induce stresses at the substrate-film interface. This, combined with the layered nature of Sb_2Te_3, can results in film delamination during the fabrication process.[18,43] On the other hand, since the layered nature of these materials is what we are trying to exploit, the only factor on which we can work to mitigate delamination is the RT-deposited seed. Interestingly, depositing a 3 nm thick Sb_2Te_3 seed layer at high temperature yields a film (XRD curve shown in Figure 5c) that exhibits the typical CSL features. Despite this, such peaks and satellites are less intense than those observed in case CSL deposited with the standard seed, indicating an overall lower material quality. Additionally, two minor peaks related to non (00.ℓ) GST reflections are detected, suggesting the occurrence of intermixing phenomena that lead to formation of a fraction of non-oriented GST. These non-(00.ℓ) features vanish if the high-T seed is deposited 2 nm thicker, as reported in Figure 5c, implying that with a thicker seed a better control over the layer growth is achieved.

It is important to note that, even in this case, the overall intensity and definition of XRD peaks are lower compared to CSL deposited on the standard seed. This suggests that the structural and interface quality are likely worse than for CSL deposited on the RT seed. However, a layered structure with properly oriented vdW gaps is still obtained, meaning that if the RT-seed route cannot be followed due to delamination, sacrificing some structural quality could be a viable option to successfully carry out device fabrication.

Another interesting aspect to investigate is the relationship between optical properties and CSL periodicity. In this regard, we realized a series of CSL featuring different periodicities (Λ) on SiO_2 coated with RT-deposited seed layer. The as grown films were characterized via spectroscopic ellipsometry while the relevant parameters were extracted fitting the raw data with a generated model. Further details can be found in the Experimental Section. Interestingly, regardless of the period, we measured E_{gap} values falling within a rather narrow energy range (0.3–0.34 eV), which align with previous reports on GeTe/Sb_2Te_3 superlattices.[44,45] These values, reported in **Table 1**, are reasonable considering the bandgap energies of pure GST (≃ 0.4 eV) and Sb_2Te_3 (≃ 0.17 eV),[46,47] possibly suggesting that the E_{gap} of CSLs could depend on the relative amounts of GST and Sb_2Te_3 in the films, and thus within each period. Within the limits of our model, we do not observe a correlation between E_{gap} and CSL period. Notably, the lowest E_{gap} is obtained for $\Lambda = 4$ nm Sb_2Te_3/3.6 nm GST, which is the GST-richest superlattice we measured. A similar behavior is observed for the refractive index (n) and the extinction coefficient (k), as shown in **Figure 6**.

© 2025 The Author(s). Advanced Materials Interfaces published by Wiley-VCH GmbH

21967350, 0, Downloaded from https://advanced.onlinelibrary.wiley.com/doi/10.1002/admi.202500058 by Cochraneltalia, Wiley Online Library on [09/05/2025]. See the Terms and Conditions (https://onlinelibrary.wiley.com/terms-and-conditions) on Wiley Online Library for rules of use; OA articles are governed by the applicable Creative Commons License

ADVANCED MATERIALS INTERFACES
Open Access
www.advmatinterfaces.de

Table 1. Energy gap E_{gap} and transition energy E_n extracted from ellipsometry measurements of superlattices of varying periods Λ.

Λ Sb_2Te_3/GST [nm/nm]	E_{gap} [eV]	E_n [eV]
4/1.8	0.31	1.50
4/3.6	0.30	1.50
6/3.6	0.32	1.56
9/5.4	0.34	1.54

We observed only minor variations between CSLs with different periodicities, with no clear trend emerging as a function of Λ. This indicates that factors other than the simple proportion of GST and Sb_2Te_3 might influence the optical properties of these superlattices.

We further assessed the growth of superlattices on a carbon-based film, which is becoming increasingly important for PCM devices. In fact, this film serves a dual purpose: first, it acts as a projection layer that minimizes the effects of resistance drift; second, it enhances the adhesion between the active material and the electrode, reducing the risk of delamination during integration.[48] To that end, CSL films 57 nm thick consisting of 12 repetitions of 3 nm Sb_2Te_3/1.8 nm GST were grown under identical *(p,T)* conditions on both SiO_2 and the carbon-based film using a RT-deposited seed layer. The corresponding XRD curves (see **Figure** 7a) show the distinctive CSL peaks, including the main CSL diffraction order and its related satellite peaks. This indicates that CSLs can be successfully sputter-grown on carbon-based substrates. This is further evidenced on high-resolution STEM micrograph (see micrograph in Figure 7b), which clearly shows the presence of vdW gaps throughout the entire cross section of the film. However, the zoomed micrograph in Figure 7c reveals that locally the nominal Sb_2Te_3/GST periodicity is not

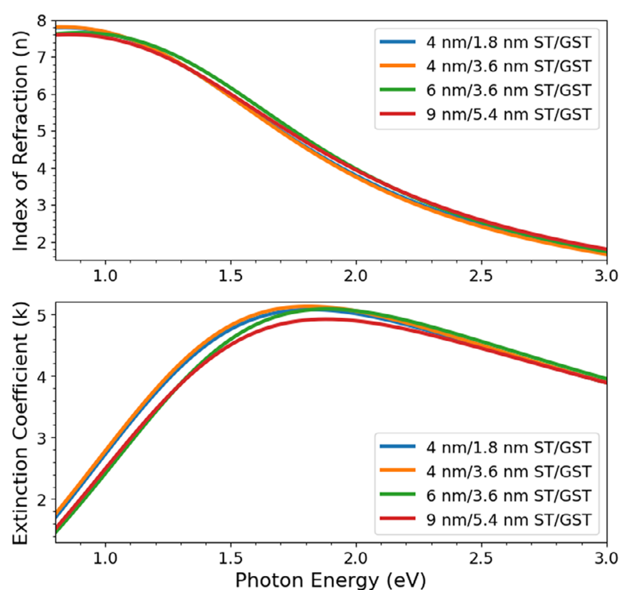

Figure 6. Index of refraction *n* and extinction coefficient *k* extracted from spectroscopic ellipsometry measurements of superlattices of different periods Λ.

always maintained. By counting the number of Te and Ge/Sb planes, we can identify blocks constituted by five atomic layers (Sb_2Te_3 QLs, blue) as well as blocks with 7, 9, and 11 Te/Ge/Sb planes, indicating the formation of GST124, 225, and 326 blocks. This variation is likely due to the fact that, although GST is less prone to intermixing compared to GeTe,[25] its intrinsic compositional disorder and tendency to form blocks of different sizes[49] allow neighboring Sb_2Te_3 and GST blocks to react and form new blocks of different compositions. An example of this is schematized in Figure 7c, where an ideal nominal stacking sequence of 3 nm Sb_2Te_3 (three blocks) and1.8 nm GST (one 225 block) is altered by interface reactions, leading to mixed blocks. Therefore, since such intermixing could alter the nominal stacking sequence, these phenomena should be considered, especially when growing CSL with smaller periods.

To evaluate the electrical properties of CSL, we measured the in-plane ($\rho_\parallel$) and cross-plane ($\rho_\perp$) electrical resistivity using a modified-Transfer Length Measurements (m-TLM). Unlike standard TLM, which only estimate in-plane resistivity, m-TLM uniquely involves creating variable resistances by etching the film to different thicknesses (*h*). This is depicted in **Figure** 8a. In our m-TLM structures (see Supporting Information Section S4 for fabrication details), the CSL remains always capped and the contacts with electrodes are always intact. This is fundamentally different from previous studies,[11] in which the film surface is exposed to ambiance (thus, oxidation) during device fabrication. The total resistance measured between the two contacts can be written as $R_{total} = 2R_c + 2R_\perp + R_\parallel$ where R_c is the contact resistance with the electrodes, $R_\perp$ is the cross-plane resistance from CSL, and $R_\parallel$ is the in-plane resistance of CSL.

Figure 8b shows an exemplar plot of R_{total} as a function of the channel length (L) for a superlattice 96 nm thick progressively etched to vary the values of *h*. We first note that the increase in measured electrical resistance as a function of *L* is perfectly linear up to 40 µm (the maximum pad distance), indicating excellent long-range uniformity of our films. $\rho_\parallel$ is computed from the slopes of these $R_{total}(L)$ curves, taking the value $\rho_\parallel = 1.19 \pm 0.02 \times 10^{-3}$ Ωcm (average of $\rho_\parallel$ extracted from each curve: 0.99×10^{-3} Ωcm, 1.15×10^{-3} Ωcm and 1.44×10^{-3} Ωcm). This value is in line with superlattices data reported in literature, as shown in the supporting information.

In principle, modified TLM also allows to assess $\rho_\perp$ by plotting the intercepts (*q*) of these $R_{total}(L)$ curves as a function of *h*. Calculating the $\rho_\perp$ with this approach in the supplementary information, we obtain, as expected, a $\rho_\perp$ value higher than $\rho_\parallel$. However, the measured $\rho_\perp$ is also significantly higher than values previously reported in the literature. This discrepancy may arise from surface oxidation on the structure's sidewalls during fabrication, which could also impact the contact resistivity (ρ_c). Therefore, both $\rho_\perp$ and ρ_c could be misrepresented and further investigations are needed. A discussion and a comparison to literature are provided in the supplementary information.

3. Conclusion

In summary, we have investigated the effects of growth parameters, such as pressure and temperature, on the sputter deposition of GST, Sb_2Te_3, and their superlattices (CSL). The seed layer of a specific thickness was critical for achieving oriented growth,

© 2025 The Author(s). Advanced Materials Interfaces published by Wiley-VCH GmbH

21967350, 0, Downloaded from https://advanced.onlinelibrary.wiley.com/doi/10.1002/admi.202500058 by Cochraneltalia, Wiley Online Library on [09/05/2025]. See the Terms and Conditions (https://onlinelibrary.wiley.com/terms-and-conditions) on Wiley Online Library for rules of use; OA articles are governed by the applicable Creative Commons License

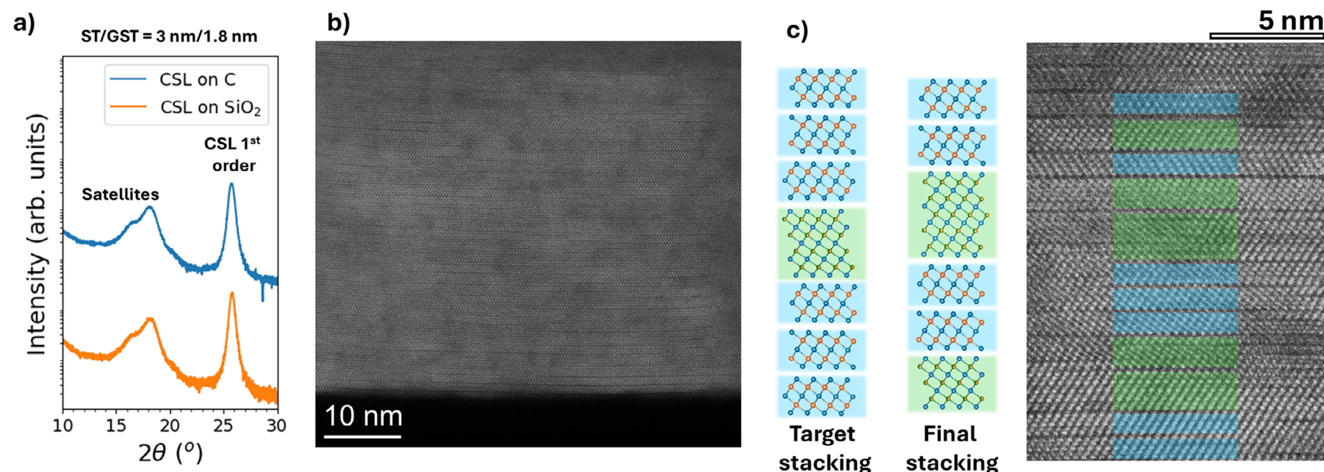

Figure 7. a) XRD curves of Sb_2Te_3/GST superlattices deposited on SiO_2 (orange) and on a C-based layer (blue) films. b) A TEM micrograph showing the persistence of vdW gaps throughout the entire superlattice stack; c) Schematic representation of nominal and final CSL stacking with and without local intermixing at the interface compared with detailed micrograph showing Sb_2Te_3 (light blue) and GST (light green) blocks.

with pressure being particularly important for Sb_2Te_3 due to its impact on Te desorption. In this context, additional TEM measurements on Sb_2Te_3 could offer further insights into Sb accumulation as a function of pressure. For GST, deposition optimization enabled control over the stacking of the cubic phase, as well as the growth of t-GST, without altering the target composition, with temperature being the most influential factor. This is particularly relevant in light of renewed interest in textured GST as active material.[43,50] A *p,T* diagram was developed to map optimal growth conditions for these films, resulting in highly textured and uniform growth of CSL films with varying periodicities on relevant substrates. CSL growth was also achieved using a seed layer deposited at high T, useful to minimize potential delamination. Atomic characterization revealed local intermixing at the interfaces. Characterization of the optical refractive indices showed no dependency on periodicity. The quality of interfaces could be explained by deposition defined desorption kinetics and film roughness. These results provide a directed methodology for sputter growth of CSL as well as textured Sb_2Te_3 and GST. Finally, it would be interesting to explore how the structure and intermixing in superlattice films influence the electrical behavior of memory devices, for example on the programming efficiency and endurance. This is in the interest of a future work.

4. Experimental Section

The sputter deposition of the films were carried out using FHR.Star.75.Co DC magnetron sputtering tool. Single GST 225 and Sb_2Te_3 stoichiometric targets were used, and depositions were carried out with ≃ low 10^{-7} µbar base pressure. Films were deposited on 20 mm × 20 mm Si(100) chips covered by ≃100 nm thick bare, and amorphous carbon coated, thermal SiO_2. Prior to material deposition, each substrate was cleaned with acetone and isopropanol for 10 ' and in-situ with Ar+ inverse sputtering etching (ISE) process to remove native oxide. Deposition rates of Sb_2Te_3 and GST films were evaluated via X-ray reflectivity measurements. To maintain low deposition rate, 30 W sputtering power was used. Depending on

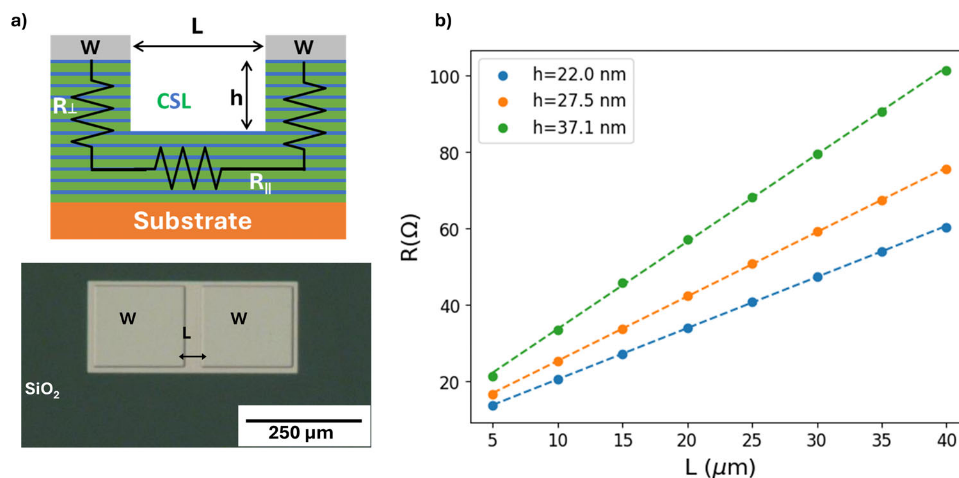

Figure 8. a) Cross section schematizing of the structures realized for m-TLM measurements and top view from optical microscope after fabrication; b) R(L) measurements (dots) and related linear fit (dashed lines) of CSL featuring different etch depth *h*.

© 2025 The Author(s). Advanced Materials Interfaces published by Wiley-VCH GmbH

21967350, 0, Downloaded from https://advanced.onlinelibrary.wiley.com/doi/10.1002/admi.202500058 by Cochraneltalia, Wiley Online Library on [09/05/2025]. See the Terms and Conditions (https://onlinelibrary.wiley.com/terms-and-conditions) on Wiley Online Library for rules of use; OA articles are governed by the applicable Creative Commons License

the subsequent processing steps, samples were capped in situ either with SiO_2 or W. Out of plane diffraction curves were acquired in $\theta-2\theta$ symmetric geometry using Bruker D8 discovery diffractometer mounting Cu anode and using Kα radiation (λ = 1.5406 Å). Ellipsometry measurements were performed in a J.A. Wollam spectroscopic elllipsometer. Data collected at room temperature at three incidence angles (60°, 65°, and 70°). Optical constants and other relevant parameters were extracted by fitting experimental data to a Tauc–Lorentz oscillator model[51,52] on WVASE software package. Each sample was simulated with a layered model featuring one layer for the substrate, one for the active material and one for the capping layer and/or surface roughness. Imaging was performed using a probe- and image-corrected ThermoFisher Scientific ThemisZ S/TEM microscope operated at 300 kV in STEM mode. A current of approximately 20 pA was used not to destroy the phase-change material, at a convergence angle of approximately 25 mrad. The detectors used were a high-angle annular dark-field (HAADF) detector, a four-segment annular detector (DF4) for integrated differential phase contrast (iDPC). For the images, the dwell time was set to 2 µs for a 4096 × 4096 pixel resolution. The elemental maps of 1024 × 1024 pixels were collected with drift correction over several hours to get sufficient counts with the low current.

Supporting Information

Supporting Information is available from the Wiley Online Library or from the author.

Acknowledgements

This work was supported by the IBM Research AI Hardware Center. The authors would like to express their gratitude to the Binnig and Rohrer Nanotechnology Center (BRNC). S.P. would like to thank Prof. Stefano Cecchi for insightful discussions on XRD and to Prof. Fabio de Matteis for his support with ellipsometry data analysis.

Conflict of Interest

The authors declare no conflict of interest.

Author Contributions

G.S.S. defined the research question and direction. S.P. conceived the methodology and performed the film depositions, experiments and data analysis. V.P.J. contributed with the film deposition and V.B. and J.L. contributed with the spectroscopy, X-ray diffraction and microscopy of the films. B.J.K. and F.A. contributed to the metrology measurements. A.S. and G.S.S. supervised the project. S.P. and G.S.S. wrote the manuscript with inputs from all authors.

Data Availability Statement

The data that support the findings of this study are available from the corresponding author upon reasonable request.

Keywords

phase change materials, superlattice films, nanodevices

Received: January 20, 2025
Revised: February 24, 2025
Published online:

[1] A. Sebastian, M. Le Gallo, G. W. Burr, S. Kim, M. BrightSky, E. Eleftheriou, *J. Appl. Phys.* **2018**, *124*, 11.
[2] M. Le Gallo, R. Khaddam-Aljameh, M. Stanisavljevic, A. Vasilopoulos, B. Kersting, M. Dazzi, G. Karunaratne, M. Brändli, A. Singh, S. M. Mueller, J. Büchel, X. Timoneda, V. Joshi, M. J. Rasch, U. Egger, A. Garofalo, A. Petropoulos, T. Antonakopoulos, K. Brew, S. Choi, I. Ok, T. Philip, V. Chan, C. Silvestre, I. Ahsan, N. Saulnier, V. Narayanan, P. A. Francese, E. Eleftheriou, A. Sebastian, *Nat. Electron.* **2023**, *6*, 680.
[3] G. W. Burr, M. J. Brightsky, A. Sebastian, H.-Y. Cheng, J.-Y. Wu, S. Kim, N. E. Sosa, N. Papandreou, H.-L. Lung, H. Pozidis, E. Eleftheriou, C. Lam, *IEEE J. Emerging Sel. Top. Circuits Syst.* **2016**, *6*, 146.
[4] S. Ghazi Sarwat, T. M. Philip, C.-T. Chen, B. Kersting, R. L. Bruce, C.-W. Cheng, N. Li, N. Saulnier, M. BrightSky, A. Sebastian, *Adv. Funct. Mater.* **2021**, *31*, 2106547.
[5] W. W. Koelmans, A. Sebastian, V. P. Jonnalagadda, D. Krebs, L. Dellmann, E. Eleftheriou, *Nat. Commun.* **2015**, *6*, 8181.
[6] R. E. Simpson, P. Fons, A. V. Kolobov, T. Fukaya, M. Krbal, T. Yagi, J. Tominaga, *Nat. Nanotechnol.* **2011**, *6*, 501.
[7] J. Momand, R. Wang, J. E. Boschker, M. A. Verheijen, R. Calarco, B. J. Kooi, *Nanoscale* **2015**, *7*, 19136.
[8] R. Wang, V. Bragaglia, J. E. Boschker, R. Calarco, *Cryst. Growth Des.* **2016**, *16*, 3596.
[9] D. Térébénec, N. Castellani, N. Bernier, V. Sever, P. Kowalczyk, M. Bernard, M.-C. Cyrille, N.-P. Tran, F. Hippert, P. Noé, *Physica Status Solidi (RRL)–Rapid Research Letters* **2021**, *15*, 2000538.
[10] M. Boniardi, J. E. Boschker, J. Momand, B. J. Kooi, A. Redaelli, R. Calarco, *Physica Status Solidi (RRL)–Rapid Research Letters* **2019**, *13*, 1800634.
[11] H. Kwon, A. I. Khan, C. Perez, M. Asheghi, E. Pop, K. E. Goodson, *Nano Lett.* **2021**, *21*, 5984.
[12] B. J. Kooi, M. Wuttig, *Adv. Mater.* **2020**, *32*, 1908302.
[13] J.-J. Wang, J. Wang, Y. Xu, T. Xin, Z. Song, M. Pohlmann, M. Kaminski, L. Lu, H. Du, C.-L. Jia, R. Mazzarello, M. Wuttig W. Zhang, *Physica Status Solidi (RRL)–Rapid Research Letters* **2019**, *13*, 1900320.
[14] B. Kooi, J. T. M. De Hosson, *J. Appl. Phys.* **2002**, *92*, 3584.
[15] A. I. Khan, X. Wu, C. Perez, B. Won, K. Kim, P. Ramesh, H. Kwon, M. C. Tung, Z. Lee, I.-K. Oh, K. Saraswat, M. Asheghi, K. E. Goodson, H-S P. Wong, E. Pop, *Nano Lett.* **2022**, *22*, 6285.
[16] Y. Saito, P. Fons, A. V. Kolobov, K. V. Mitrofanov, K. Makino, J. Tominaga, S. Hatayama, Y. Sutou, M. Hase, J. Robertson, *J. Phys. D Appl. Phys.* **2020**, *53*, 284002.
[17] P. Kowalczyk, F. Hippert, N. Bernier, C. Mocuta, C. Sabbione, W. Batista-Pessoa, P. Noé, *Small* **2018**, *14*, 1704514.
[18] J. E. Boschker, E. Tisbi, E. Placidi, J. Momand, A. Redaelli, B. J. Kooi, F. Arciprete, R. Calarco, *AIP Adv.* **2017**, *7*, 015106.
[19] C. Yoo, J. W. Jeon, S. Yoon, Y. Cheng, G. Han, W. Choi, B. Park, G. Jeon, S. Jeon, W. Kim, Y. Zheng, J. Lee, J. Ahn, S. Cho, S. B. Clendenning, I. V. Karpov, Y. K. Lee, J-H. Choi, C. S. Hwang, *Adv. Mater.* **2022**, *34*, 2207143.
[20] R.-J. Zhu, R.-Z. Zhao, K. Gao, Z.-R. Zhang, Q. He, H. Tong, X.-S. Miao, *Adv. Funct. Mater.* **2024**, *34*, 2408897.
[21] J. K. Behera, X. Zhou, A. Ranjan, R. E. Simpson, *ACS Appl. Mater. Interfaces* **2018**, *10*, 15040.
[22] C. Yoo, J. W. Jeon, B. Park, W. Choi, G. Jeon, S. Jeon, S. Kim, C. S. Hwang, *ACS Appl. Electron. Mater.* **2023**, *5*, 5794.
[23] S. Cremer, L. Voß, N. Braun, N. Wolff, L. Kienle, A. Lotnyk, *Appl. Surf. Sci.* **2024**, *655*, 159679.
[24] J. Feng, A. Lotnyk, H. Bryja, X. Wang, M. Xu, Q. Lin, X. Cheng, M. Xu, H. Tong, X. Miao, *ACS Appl. Mater. Interfaces* **2020**, *12*, 33397.
[25] S. Cecchi, E. Zallo, J. Momand, R. Wang, B. J. Kooi, M. A. Verheijen, R. Calarco, *APL Mater.* **2017**, *5*, 2.
[26] A. I. Khan, C. Perez, X. Wu, B. Won, K. Kim, H. Kwon, P. Ramesh, K. M. Neilson, M. Asheghi, K. Saraswat, Z. Lee, I.-K. Oh, H.-S. P. Wong,

© 2025 The Author(s). Advanced Materials Interfaces published by Wiley-VCH GmbH

21967350, 0, Downloaded from https://advanced.onlinelibrary.wiley.com/doi/10.1002/admi.202500058 by Cochraneltalia, Wiley Online Library on [09/05/2025]. See the Terms and Conditions (https://onlinelibrary.wiley.com/terms-and-conditions) on Wiley Online Library for rules of use; OA articles are governed by the applicable Creative Commons License

K. E. Goodson, E. Pop, in *2022 IEEE Symposium on VLSI Technology and Circuits (VLSI Technology and Circuits)*, IEEE, **2022**, pp. 310–311.
[27] X. Wu, A. I. Khan, H. Lee, C.-F. Hsu, H. Zhang, H. Yu, N. Roy, A. V. Davydov, I. Takeuchi, X. Bao, H-S P. Wong, E. Pop, *Nat. Commun.* **2024**, *15*, 13.
[28] Y. Saito, P. Fons, L. Bolotov, N. Miyata, A. V. Kolobov, J. Tominaga, *AIP Adv.* **2016**, *6*, 045220.
[29] S. Cecchi, D. Dragoni, D. Kriegner, E. Tisbi, E. Zallo, F. Arciprete, V. Holý, M. Bernasconi, R. Calarco, *Adv. Funct. Mater.* **2019**, *29*, 1805184.
[30] D. T. Yimam, M. Ahmadi, B. J. Kooi, *Mater. Today Nano* **2023**, *23*, 100365.
[31] V. Bragaglia, K. Holldack, J. Boschker, F. Arciprete, E. Zallo, T. Flissikowski, R. Calarco, *Sci. Rep.* **2016**, *6*, 28560.
[32] T. L. Anderson, H. B. Krause, *Acta Crystallographica Section B: Structural Crystallography and Crystal Chemistry* **1974**, *30*, 1307.
[33] T. Matsunaga, N. Yamada, Y. Kubota, *Acta Crystallogr., Sect. B: Struct. Sci.* **2004**, *60*, 685.
[34] J. L. Da Silva, A. Walsh, H. Lee, *Physical Review B–Condensed Matter and Materials Physics* **2008**, *78*, 224111.
[35] W. Zhang, A. Thiess, P. Zalden, R. Zeller, P. Dederichs, J.-Y. Raty, M. Wuttig, S. Blügel, R. Mazzarello, *Nat. Mater.* **2012**, *11*, 952.
[36] V. Bragaglia, F. Arciprete, W. Zhang, A. M. Mio, E. Zallo, K. Perumal, A. Giussani, S. Cecchi, J. E. Boschker, H. Riechert, S. Privitera, E. Rimini, R. Mazzarello, R. Calarco, *Sci. Rep.* **2016**, *6*, 23843.
[37] T. Siegrist, P. Jost, H. Volker, M. Woda, P. Merkelbach, C. Schlockermann, M. Wuttig, *Nat. Mater.* **2011**, *10*, 202.
[38] V. Bragaglia, F. Arciprete, A. M. Mio, R. Calarco, *J. Appl. Phys.* **2018**, *123*, 215304.
[39] S. Cecchi, J. Momand, D. Dragoni, O. Abou El Kheir, F. Fagiani, D. Kriegner, C. Rinaldi, F. Arciprete, V. Holý, B. J. Kooi, M. Bernasconi, R. Calarco, *Adv. Sci.* **2024**, *11*, 2304785.
[40] I. Hilmi, A. Lotnyk, J. W. Gerlach, P. Schumacher, B. Rauschenbach, *Mater. Des.* **2017**, *115*, 138.
[41] V. Bragaglia, B. Jenichen, A. Giussani, K. Perumal, H. Riechert, R. Calarco, *J. Appl. Phys.* **2014**, *116*, 054913.
[42] M. Bertelli, A. Díaz Fattorini, S. De Simone, S. Calvi, R. Plebani, V. Mussi, F. Arciprete, R. Calarco, M. Longo, *Nanomaterials* **2022**, *12*, 2001.
[43] G. Cohen, A. Majumdar, C. Cheng, A. Ray, D. Piatek, L. Gignac, C. Lavoie, A. Grun, H. Cheng, Z. Liu, H. Lung, H. Miyazoe, R. L. Bruce, M. BrightSky, *Physica Status Solidi (RRL)–Rapid Research Letters* **2024**, *18*, 2300426.
[44] A. Caretta, B. Casarin, P. Di Pietro, A. Perucchi, S. Lupi, V. Bragaglia, R. Calarco, F. R. L. Lange, M. Wuttig, F. Parmigiani, M. Malvestuto, *Phys. Rev. B* **2016**, *94*, 045319.
[45] J. E. Boschker, X. Lü, V. Bragaglia, R. Wang, H. T. Grahn, R. Calarco, *Sci. Rep.* **2018**, *8*, 5889.
[46] P. Němec, A. Moreac, V. Nazabal, M. Pavlišta, J. Přikryl, M. Frumar, *J. Appl. Phys.* **2009**, *106*, 103509.
[47] J.-W. Park, S. H. Eom, H. Lee, J. L. Da Silva, Y.-S. Kang, T.-Y. Lee, Y. H. Khang, *Physical Review B–Condensed Matter and Materials Physics* **2009**, *80*, 115209.
[48] G. S. Syed, K. Brew, A. Vasilopoulos, V. P. Jonnalagadda, B. Kersting, T. Philip, V. Bragaglia, S. Ambrogio, J. Bučhel, I. Giannopoulos, M. Le Gallo, C.-W. Cheng, M. BrightSky, V. Narayanan, N. Saulnier, A. Sebastian, *2023 International Electron Devices Meeting (IEDM)*, IEEE, **2023**, pp. 1–4.
[49] A. M. Mio, S. M. Privitera, V. Bragaglia, F. Arciprete, C. Bongiorno, R. Calarco, E. Rimini, *Nanotechnology* **2017**, *28*, 065706.
[50] D. Térébénec, F. Hippert, N. Bernier, N. Castellani, P. Noé, *Adv. Electron. Mater.* **2024**, 2400290.
[51] G. Jellison Jr, F. Modine, *Appl. Phys. Lett.* **1996**, *69*, 371.
[52] G. Jellison, F. Modine, *Appl. Phys. Lett.* **1996**, *69*, 2137.

© 2025 The Author(s). Advanced Materials Interfaces published by Wiley-VCH GmbH

21967350, 0, Downloaded from https://advanced.onlinelibrary.wiley.com/doi/10.1002/admi.202500058 by Cochraneltalia, Wiley Online Library on [09/05/2025]. See the Terms and Conditions (https://onlinelibrary.wiley.com/terms-and-conditions) on Wiley Online Library for rules of use; OA articles are governed by the applicable Creative Commons License

ADVANCED MATERIALS INTERFACES
Open Access

Supporting Information

for *Adv. Mater. Interfaces*, DOI 10.1002/admi.202500058

Understanding the Growth and Properties of Sputter-Deposited Phase-Change Superlattice Films

Simone Prili, Valeria Bragaglia, Vara Prasad Jonnalagadda, Jesse Luchtenveld, Bart J. Kooi, Fabrizio Arciprete, Abu Sebastian* and Ghazi Sarwat Syed**

Understanding the Growth and Properties of Sputter-Deposited Phase-Change Superlattice Films

Simone Prili,[1,2,3] Valeria Bragaglia,[1] Vara Prasad Jonnalagadda,[1] Jesse Luchtenveld,[1,4] Bart J. Kooi,[4] Fabrizio Arciprete,[2,3] Abu Sebastian,[1] and Ghazi Sarwat Syed[1]

[1)] *IBM Research – Europe, Säumerstrasse 4, 8803 Rüschlikon, Switzerland*

[2)] *Department of physics, University of Rome "Tor Vergata", Via della Ricerca Scientifica 1, 00133 Rome, Italy*

[3)] *Institute for Microelectronics and Microsystems (CNR–IMM), Via del Fosso del Cavaliere 100, 00133 Rome, Italy*

[4)] *Zernike Institute for Advanced Materials, University of Groningen, Nijenborgh 4, 9747 AG Groningen, Netherlands*

S1. AN UNDERSTANDING OF THE SEED LAYER

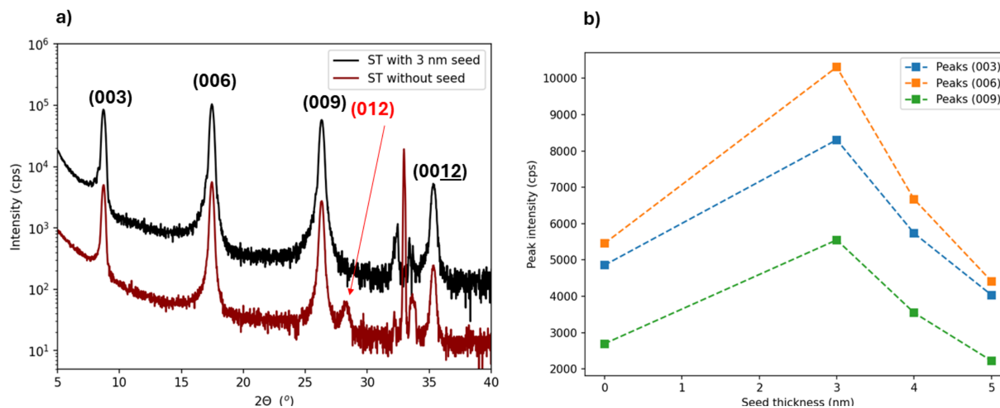

FIG. 1: **a)** Sb_2Te_3 films grown in identical conditions with and without seed layer; **b)** Intensity of (00ℓ) XRD peaks plotted as function of the thickness of the seed layer employed for the growth of the related film

In the Section detailing Sb_2Te_3 in the main text, we noted that using an Sb_2Te_3 seed layer enables a highly textured growth. Here we discuss this further. The effect of the seed layer was investigated by initially depositing $\simeq 25$ nm Sb_2Te_3 on SiO_2 under identical conditions, with and without a 3 nm thick Sb_2Te_3 seed. The XRD curves of the resulting films are shown in Figure 1a. In both cases, crystalline films were achieved. Notably, the film deposited using the seed layer was completely out-of-plane oriented, as indicated by the presence of (00ℓ) diffraction peaks. In contrast, when no seed layer was used, the Sb_2Te_3 still grew predominantly oriented, but a minor component of misoriented Sb_2Te_3 was also formed. This can be inferred from the appearance of the (012) peak, which is the most favored orientation in Sb_2Te_3 powders. Figure 1b shows the intensity of (00ℓ) diffraction peaks from films deposited under identical conditions but with seed layers of varying thicknesses. The data indicate that the highest number of counts (XRD peaks intensity) was achieved with a 3 nm thick seed layer, corresponding to three quintuple layers stacked one on top of the other. This suggests that a 3 nm seed layer provides the optimal thickness for achieving high-quality crystalline Sb_2Te_3 films.

S2. AN UNDERSTANDING OF THE TYPE OF GST BLOCKS

In the Section discussing Ge-Sb-Te in the main text, we calculated the predominant stacking sequence of c-GST by fitting VLp in the diffraction curves. Here, we present the detailed description and results of these fittings. It is well established in the literature that XRD is a valuable tool for determining the predominant stacking of c-GST[1,2]. This involves fitting the GST(111)/GST(222) XRD peaks along with the VLp feature. Typically, the main GST features are modeled using a pseudo-Voigt function, while the VLp is fitted with one or more Gaussian curves. Given that the second-order diffraction peak of the VLp is usually more intense than the first, our analysis focuses on fitting the GST(222) peak and its associated VLp. After fitting the XRD curve, the stacking (S) is calculated based on the distance Δq between the GST(222) peak and the Gaussian used to fit the VLp, according to the relation $S = 2\pi/\Delta q$.

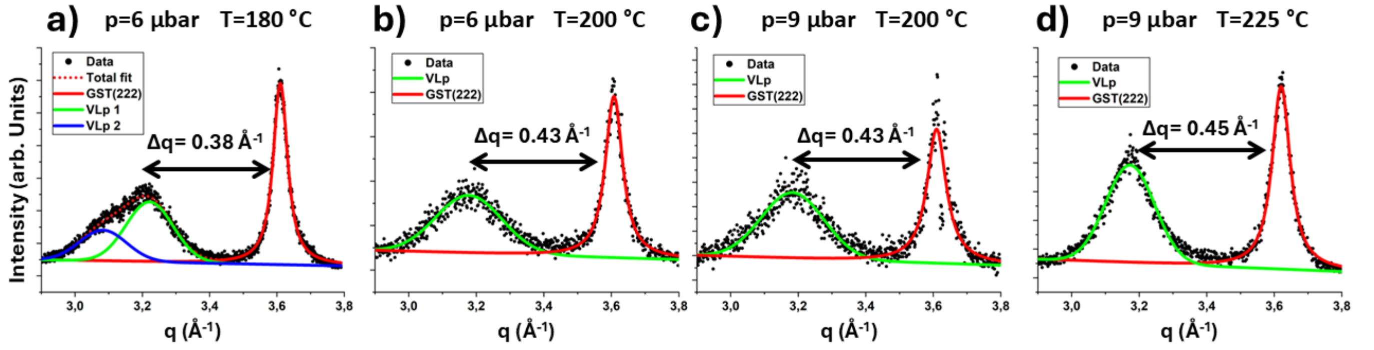

FIG. 2: XRD curves, and related fits, of GST films grown in different conditions: 180 °C and 6 μbar **(a)**; 200 °C and 6 μbar **(b)**; 200 °C and 9 μbar **(c)**; 225 °C and 9 μbar **(d)**. Red curves are pseudo-Voigts functions used to fit GST(222) reflections while green and blue curves are Gaussian for VLp modeling

The results of this analysis are shown in Figure 2, illustrating the some of the cases described in the main text. For films deposited at 6 μbar, two Gaussians are required to model the VLp of GST grown at 180 °C, while only one Gaussian is sufficient for the film deposited at 200 °C. By computing the Δq distance between the GST and VLp peaks for the film grown at 180 °C ($\Delta q = 0.38$ Å^{-1} and 0.5 Å^{-1}), results in blocksizes compatible with mixed 124/225-predominant 225 stacking[3]. Similar results are obtained with films grown under 4 μbar at 180-200 °C. Conversely, complete 124 stacking is observed under 6 μbar at 200 °C and under 9 μbar at both 200 °C and 225 °C, as proved by the single-component VLp located at $\Delta q \simeq$ 0.43-0.45 Å^{-1} .

S3. AN UNDERSTANDING OF THE EFFECT OF PRESSURE ON CSL STRUCTURE AND MORPHOLOGY

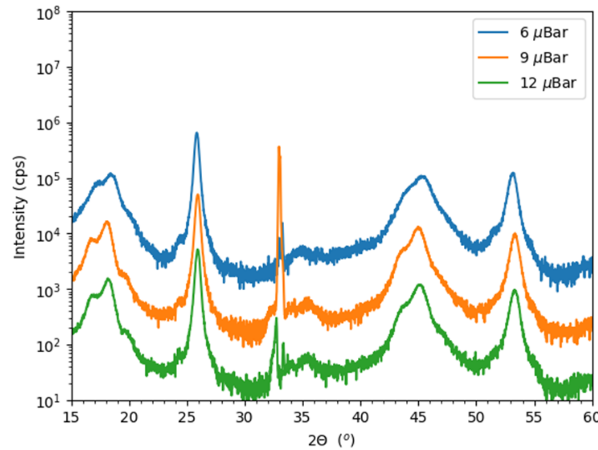

FIG. 3: XRD curves of CSL grown at 200°C under different pressure conditions

In the Section detailing CSL growth in the main text, we discussed the effect of growth pressure on the superlattices. Here, we present the XRD curves along with additional AFM and SEM data. The effect of pressure on CSL films was evaluated by growing them at 200 °C under different increasing pressures. The XRD curves reported in Figure 3 show no spurious signals from segregated unoriented GST/ Sb_2Te_3, while the first and second orders of diffraction of the CSL are very clear. Qualitative information about the structural quality can be deduced from the satellite peaks observed on the left of the main CSL peaks. As the pressure decreases, these peaks change modestly from 12 μbar to 9 μbar, while a clear broadening is observed in the film grown at 6 μbar. This is not surprising considering that Sb_2Te_3 experiences Te desorption at 6 μbar while it remains stoichiometric at 9 μbar or above. Therefore, since Te depletion causes broader CSL peaks[4], we can attribute this broadening to Te loss in Sb_2Te_3.
In figure 4, we present AFM and SEM images of the surfaces of Sb_2Te_3, GST, and a superlattice, all grown under

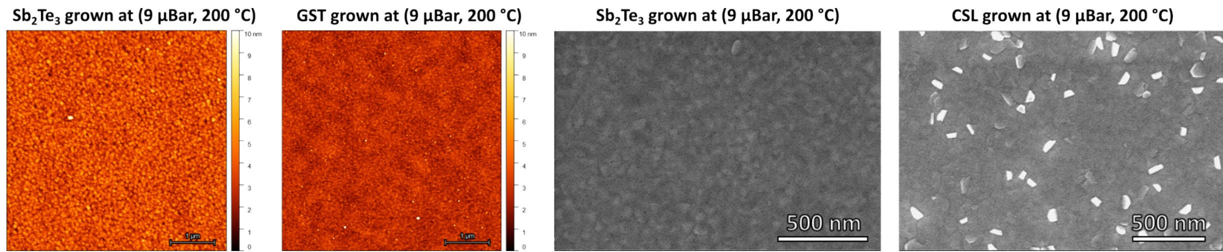

FIG. 4: SEM and AFM images of Sb_2Te_3, GST and CSL grown at 200 °C and 9 μbar

identical conditions. It is clear that while the CSL shows a number of flakes, seemingly due to delamination, the GST and Sb_2Te_3 grown under the same conditions are perfectly flat, with no signs of flaking.

S4. FABRICATION OF TLM DEVICES AND CROSS PLANE RESISTIVITY

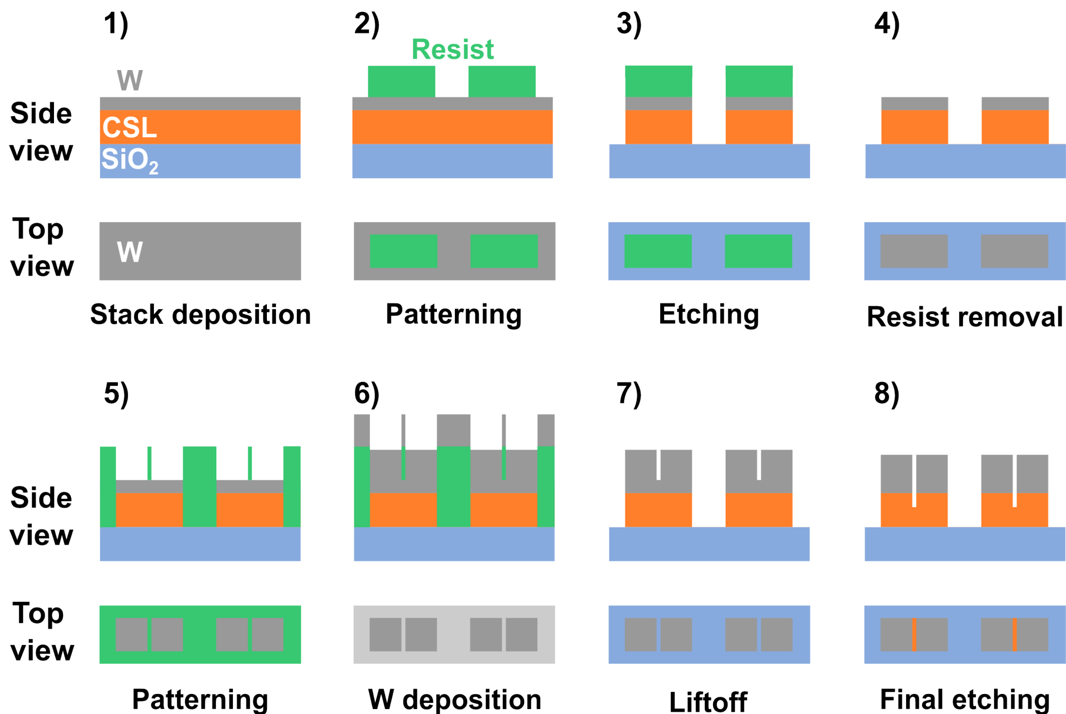

FIG. 5: Schematics of the fabrication process of the test structures used for m-TLM. The figure shows for each of the 8 steps both side view (cross section) and top view of the chip. SiO_2 substrate is blue, CSL film is orange, W is gray and the negative resist is green. Pictures not in scale.

In Section discussing electrical characterization in the main text, we presented data obtained from m-TLM to assess in-plane and cross-plane resistivity. Here, we provide a detailed description of the 8 fabrication steps schematized in Figure 5. Initially, the substrate underwent the usual chemical cleaning procedure to prepare it for film deposition. Next, the CSL film was sputter-grown on the cleaned substrate. After allowing the film to cool down, it was capped with a 10 nm layer of tungsten (W) deposited at room temperature (1). This W layer will be the starting point for the contacts and, since it is deposited in situ, it effectively prevents CSL surface exposure to atmosphere (thus oxidation). Following film deposition, the chip was removed from the growth chamber for a first lithography step that employed a negative resist to define the area of the TLM test structure (2). After the resist was developed, an ion milling etching was performed to isolate the test structures (3). The resist was then removed (4). Subsequently, another lithography step (5) with negative resist was carried out to define the pad area (100 μm $\times$100 μm). This consisted of leaving the contact area free from resist while the channel area remained covered. Subsequently, the chip was placed in a sputter tool for the deposition of100 nm W pads (6). Prior this deposition inverse sputter etch

was conducted to remove any native W oxide that may have formed (1-2 nm). The process then continued with a liftoff that removed the resists and defined the final test structures (7). A final ion milling step (8) ended the fabrication of the device, etching the remaining W in the channel as well as a portion h of the superlattice. In this way, we fabricated 80 TLM test structures, 10 for each channel length (L=5, 10, 15, 20, 25, 30, 35, 40 μm).

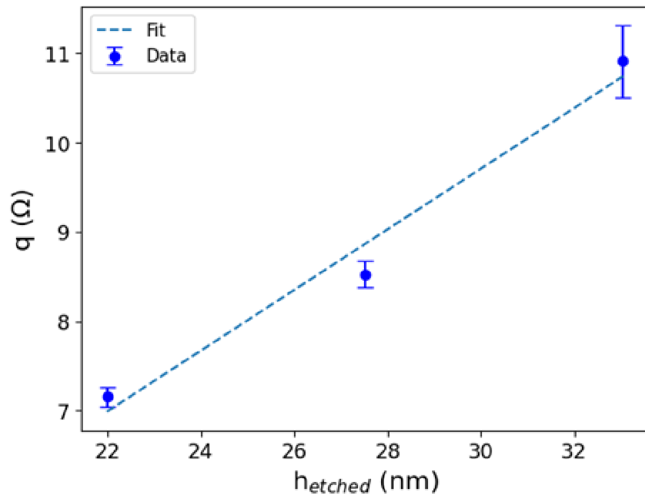

FIG. 6: Intercept $q(h_{etched})$ as function of the etch depth h and linear fit (dashed line) used for $\rho_\perp$ evaluation

TABLE I: Table reporting in plane and cross plane electrical resistivity from various superlattices reported in literature grown with various techniques

Material	In plane (Ω cm)	Cross-plane (Ω cm)	Ref.
GST/Sb_2Te_3 SL	1.19×10^{-3}	169	This work
GeTe/Sb_2Te_3 SL	5.8×10^{-4}	1.1	[5]
GeTe/Sb_2Te_3 SL	4.8×10^{-3}	19.4	[6]
In_2Se_3 nanowire SL	2×10^{-3}	40	[7]
GST/Sb_2Te_3 SL	9.2×10^{-4}		[8]

For $\rho_\perp$, the intercepts (q) of the $R_{\text{total}}(L)$ curves are plotted as a function of h and, since the intercept effectively equates to $q = 2R_c + 2\rho_\perp h/A$. Consequently, $\rho_\perp$ can be extracted from the slope of the $q(h)$ curve in Figure 6, yielding $\rho_\perp = 169 \pm 36$ Ωcm. This translates in a stark contrast between the cross-plane and in-plane resistivity, on the order of 100000 x. However, as summarized in Table I, the $\rho_\perp/\rho_\parallel$ ratio observed here is significantly higher than previous reports in the literature[5,6,8], primarily due to an unusually high cross-plane resistivity. While a substantial difference between in-plane and cross-plane conductivity is expected, such an elevated value could be influenced by additional factors. For instance, all the sidewalls of the vertical pillars, which contribute to the cross-plane resistivity, are directly exposed to the atmosphere, increasing the surface area susceptible to oxidation. This could compromise the accuracy of the cross-plane resistivity measurement. Therefore, to validate the reported $\rho_\perp$ value, further investigations are necessary to rule out the influence of such effects. Moreover, since the vertical pillars contribute also to the contact resistance, even this value is likely affected by oxidation. As a result, isolating the contact resistivity (ρ_c) from $\rho_\perp$ is not straightforward. However, for completeness, we estimate the contact resistivity using $\rho_\perp$ value reported in ref.[5], yielding 4.4×10^{-4} Ω cm^2. Conversely, $\rho_\parallel$ is less affected as the portion of film involved in the evaluation of $\rho_\parallel$ exposes much less area to the ambiance. As a result, the measured $\rho_\parallel$ value is in line with previous reports (see table I).

BIBLIOGRAPHY

[1]Bragaglia, V., Arciprete, F., Mio, A. M. & Calarco, R. Designing epitaxial GeSbTe alloys by tuning the phase, the composition, and the vacancy ordering. *Journal of Applied Physics* **123**, 215304 (2018).

[2]Bragaglia, V. *et al.* Metal-insulator transition driven by vacancy ordering in GeSbTe phase change materials. *Scientific reports* **6**, 23843 (2016).

[3]Zallo, E. *et al.* Evolution of low-frequency vibrational modes in ultrathin GeSbTe films. *Physica Status Solidi (RRL)–Rapid Research Letters* **15**, 2000434 (2021).

[4]Kowalczyk, P. *et al.* Impact of Stoichiometry on the Structure of van der Waals Layered GeTe/Sb_2Te_3 Superlattices Used in Interfacial Phase-Change Memory (iPCM) Devices. *Small* **14**, 1704514 (2018).

[5]Kwon, H. *et al.* Uncovering thermal and electrical properties of Sb_2Te_3/GeTe superlattice films. *Nano Letters* **21**, 5984–5990 (2021).

[6]Yang, Z., Xu, M., Cheng, X., Tong, H. & Miao, X. Manipulation of dangling bonds of interfacial states coupled in GeTe-rich GeTe/Sb_2Te_3 superlattices. *Scientific Reports* **7**, 17353 (2017).

[7]Peng, H., Xie, C., Schoen, D. T. & Cui, Y. Large anisotropy of electrical properties in layer-structured in2se3 nanowires. *Nano Letters* **8**, 1511–1516 (2008).

[8]Cecchi, S. *et al.* Improved structural and electrical properties in native $Sb_2Te_3/Ge_xSb_2Te_{3+x}$ van der waals superlattices due to intermixing mitigation. *APL Materials* **5** (2017).